ResearchGate

See discussions, stats, and author profiles for this publication at: https://www.researchgate.net/publication/272029461

Numerical study of two-phase fluid distributions in fractured porous media

Article *in* International Journal for Numerical and Analytical Methods in Geomechanics · February 2015

DOI: 10.1002/nag.2358

CITATIONS
6

READS
177

2 authors:

Peijie Yin
Chang'an University
11 PUBLICATIONS **35** CITATIONS
SEE PROFILE

Gaofeng Zhao
Tianjin University
108 PUBLICATIONS **1,087** CITATIONS
SEE PROFILE

Some of the authors of this publication are also working on these related projects:

Wave propagation in discontinuous rock mass View project

Dynamic behavior and response of rock, discontinuity and underground opening View project

All content following this page was uploaded by Peijie Yin on 17 October 2018.

The user has requested enhancement of the downloaded file.

INTERNATIONAL JOURNAL FOR NUMERICAL AND ANALYTICAL METHODS IN GEOMECHANICS
Int. J. Numer. Anal. Meth. Geomech. 2015; **39**:1188–1211
Published online 3 February 2015 in Wiley Online Library (wileyonlinelibrary.com). DOI: 10.1002/nag.2358

Numerical study of two-phase fluid distributions in fractured porous media

Peijie Yin and Gao-Feng Zhao*,†

Centre for Infrastructure Engineering and Safety, School of Civil and Environmental Engineering, University of New South Wales, Sydney, NSW 2052, Australia

SUMMARY

Two-phase fluid distributions in fractured porous media were studied using a single-component multiphase (SCMP) lattice Boltzmann method (LBM), which was selected among three commonly used numerical approaches through a comparison against the available results of micro X-ray computed tomography. The influence of the initial configuration and the periodic boundary conditions in the SCMP LBM for the fluid distribution analysis were investigated as well. It was revealed that regular porous media are sensitive to the initial distribution, whereas irregular porous media are insensitive. Moreover, to eliminate the influence of boundaries, the model's buffer size of an SCMP LBM simulation was suggested to be taken as approximately 12.5 times the average particle size. Then, the two-phase fluid distribution of a porous medium was numerically studied using the SCMP LBM. Both detailed distribution patterns and macroscopic morphology parameters were reasonably well captured. Finally, the two-phase fluid distributions in a fractured porous media were investigated. The influence of the degree of saturation, fracture length, and fracture width on the fluid distributions and migration was explored. Copyright © 2015 John Wiley & Sons, Ltd.

Received 7 August 2014; Revised 17 December 2014; Accepted 5 January 2015

KEY WORDS: two-phase fluid distribution; fractured porous media; lattice Boltzmann method; X-ray CT

1. INTRODUCTION

The characterization of fluid distributions is of fundamental importance to the accurate modeling of multiphase flow problems, which are related to many industrial applications, for example, radioactive disposal sites [1], oil/gas extraction [2], and contaminant transport [3]. According to a literature review [4–9], there are two types of commonly used approaches to characterize the fluid distribution in porous media: experimental and numerical approaches.

The most popular types of equipment used to visualize the phase distribution in porous media are scanning electron microscopy (SEM) and micro X-ray computed tomography (CT). Gvirtzman *et al*. [10] investigated the water phase distribution within an unsaturated porous medium using SEM. To satisfy the requirement of SEM on a dried specimen, a rapid cooling technique was adopted. However, the cooling process caused a change in the volume of the liquid and led to most of the samples being destructed. This shortcoming can be overcome using X-ray CT; for example, Schmitz *et al*. [11, 12] conducted a study on the stationary water/air distribution in random and structured packing media using high-resolution micro X-ray CT, and Wildenschild *et al*. [13]

*Correspondence to: G.-F. Zhao, Centre for Infrastructure Engineering and Safety, School of Civil and Environmental Engineering, University of New South Wales, Sydney, NSW 2052, Australia.
†E-mail: gaofeng.zhao@unsw.edu.au

Copyright © 2015 John Wiley & Sons, Ltd.

adopted X-ray CT to measure the saturation, distribution, and interfacial characteristics of the fluids within the pore space. In addition to SEM and micro X-ray CT, other techniques, such as nuclear magnetic resonance and confocal laser scanning microscopy, have also been used by a few researchers; for example, Liaw *et al*. [14] studied the pore structure and fluid phase distribution of sandstone and carbonate samples using nuclear magnetic resonance, and Krummel *et al*. [15] visualized the two immiscible fluids in a 3D porous medium using confocal laser scanning microscopy.

However, the direct exploration of the underlying microscopic multiphase distribution is time consuming and expensive. Alternatively, numerical approaches provide attractive solutions because of their advantages of low cost, high efficiency, and repeatability. Many numerical methods have been developed to predict multiphase distributions in porous media. There are two popular categories: the simulated annealing method (SAM) and the lattice Boltzmann method (LBM). The SAM is a global optimization method proposed by Kirkpatrick *et al*. [16], which can be used in the study of multiphase systems, as described in Politis *et al*. [17]. The SAM was first used to investigate the equilibrium phase distribution by Knight *et al*. [18]. Later, Silverstein and Fort [19, 20] applied the method to study the fluid distribution in sphere packs, Berkowitz and Hansen [21] extended the SAM to the water distribution in a partially saturated sandstone, and Lu *et al*. [22] investigated the capillarity phenomenon in porous media. Recently, the LBM has become a promising solution for multiphase problems for porous media [23]. Three popular multiphase LBM models have been developed [24]: the free-energy LBM, the Rothman–Keller LBM, and the Shan–Chen LBM. An extensive literature review on these models can be found in the work by Huang *et al*. [24]. Among those models, the Shan–Chen LBM [25, 26] receives the most popularity because of its well-defined inter-particle potential and straightforward implementation. There are two sub-categories in the Shan–Chen LBM: the multi-component multiphase (MCMP) LBM [25] and the single-component multiphase (SCMP) LBM [26]. The MCMP LBM model allows for fluid phases with different wettability, densities, and viscosities. The MCMP LBM was used to study the hysteretic capillary pressure–saturation of a packed-sphere system by Pan *et al*. [27], the contact angle between the fluid and solid surface in [28], and the distribution of multiphase fluids in porous media in [29]. The SCMP LBM focuses on the modeling of one-component fluid systems that obey a non-ideal gas equation of state and that can undergo a liquid–gas-type phase transition. The SCMP LBM has been successfully applied to investigate the invasion percolation in porous media [30] and the effect of gravity, adhesion, and surface tension on capillary-rise problems [31].

The aforementioned studies usually focus on qualitatively describing how the multiphase fluid is distributed in porous media; however, no quantitative study on the multiphase fluid distribution in a fractured porous media has been performed. A fracture in porous media is generally considered as a fast pathway for transports [32], but the fracture may impede the flow under partial saturation [33]. The accurate description of fluid flow in unsaturated fractured porous media requires a clear understanding of the mechanism that produces the multiphase distribution. Moreover, to our knowledge, the accuracy of these numerical methods is still unclear, and a comprehensive verification is strongly required. For example, Lu *et al*. [22] verified the prediction results of the SAM against X-ray CT observations, Sukop *et al*. [29] compared the MCMP LBM with X-ray CT results, and Sukop and Or [30] declared that SCMP LBM can produce realistic multiphase distributions. However, no work has been performed toward a quantitative comparison between these numerical approaches against the experimental observations. In this paper, a full comparison of the results predicted by the SAM, MCMP LBM, and SCMP LBM with the experimental results of micro X-ray CT [29] is discussed. It was found that the SCMP LBM shows advantages over the other two numerical methods in terms of computational efficiency and multiphase characterization. In addition, the influence of periodic boundary condition and the initial configuration on the fluid distribution predicted by the SCMP LBM were studied. Following this, the influence of the degree of saturation on the fluid distribution was investigated for an artificial porous medium that was generated using the discrete element method. Finally, the two-phase fluid distribution in a fractured porous media was studied numerically.

Copyright © 2015 John Wiley & Sons, Ltd.

DOI: 10.1002/nag

2. NUMERICAL METHODS

2.1. Simulated annealing method

To represent the fluid distribution of a porous media involving the solid, wetting, and non-wetting phases, a three-spin Ising model [34] is used.

$$\mathrm{Ising}\left(\overrightarrow{r}\right) = \begin{cases} -1 & \text{nonwetting phase} \\ 0 & \text{solid phase} \\ 1 & \text{wetting phase} \end{cases} \tag{1}$$

where $\overrightarrow{r}$ is the spatial location of a pixel (voxel).

The geometry of the solid phase is represented as a group of pixels (voxels) that are assigned to be 0. The wetting and non-wetting phases are randomly introduced in the pore space to satisfy the desirable degree of saturation.

The phase distribution of the porous media is governed by the interfacial energy. The equilibrium configuration corresponds to the system of minimum global interfacial energy. The global interfacial energy E of the system can be calculated as

$$E = \sum_{i,j}\sum_{k,\overline{k}} J_{k\overline{k}} n_i^k n_j^{\overline{k}} \tag{2}$$

which is the interfacial energy between the pixel site i and all its nearest neighbor sites j, with phases of k and $\overline{k}$ that span all the sites, where $n_i^k = 1$ if the pixel site is in phase k and 0 otherwise. $J_{k,\overline{k}}$ is the interfacial free energy of the contact surface between different phases and is defined as

$$J_{k,\overline{k}} = \begin{cases} -1 & \left(k = 1, \overline{k} = 1\right) \\ 1 & \left(k = 1, \overline{k} = -1\right) \\ -2 & \left(k = 1, \overline{k} = 0\right) \\ 0 & \text{else} \end{cases} \tag{3}$$

which reproduces the perfect wetting condition [22].

During the simulation, two randomly selected pixels of different fluid phases in the pore space will try to exchange their positions, which will result in a variation in the interfacial energy of the system ΔE. To minimize the system energy, the system is updated with a probability p to accept the pixel exchange according to the Metropolis algorithm.

$$p = \begin{cases} 1 & \Delta E \le 0 \\ e^{-\Delta E / E_{\mathrm{ref}}} & \Delta E > 0 \end{cases} \tag{4}$$

where E_{ref} is the reference energy given by a 'cooling schedule' as

$$E_{\mathrm{ref}} = f^m \cdot E_{\mathrm{ref},0} \tag{5}$$

in which f is the reduction parameter, m is the number of the Markov chain, and $E_{\mathrm{ref},0}$ is the initial value of E_{ref}. The value of f is significant in the simulation and must satisfy $0 < f < 1$. A small f indicates fast convergence but a high risk of local minima trapping. The physically sound configuration appears when f approaches 1. Meanwhile, the value of E_{ref} should be sufficiently large so that the system can approach the optimal distribution, which is chosen as approximately 30 times the highest value of $J_{k,\overline{k}}$, as shown in Politis *et al*. [17]. Therefore, $f = 0.95$ and $E_{\mathrm{ref},0} = 30$ were used in this paper.

The detailed procedure of the SAM is shown in Figure 1. The system approaches equilibrium (Figure 1(c)) when the energy change between two Markov chains satisfies $(E^m - E^{m-1})/E^{m-1} < 10^{-5}$. After reaching equilibrium, another 200 Markov chains are performed, and the profiles generated from each of the Markov chains are averaged to create a smooth curve of the

Copyright © 2015 John Wiley & Sons, Ltd.

DOI: 10.1002/nag

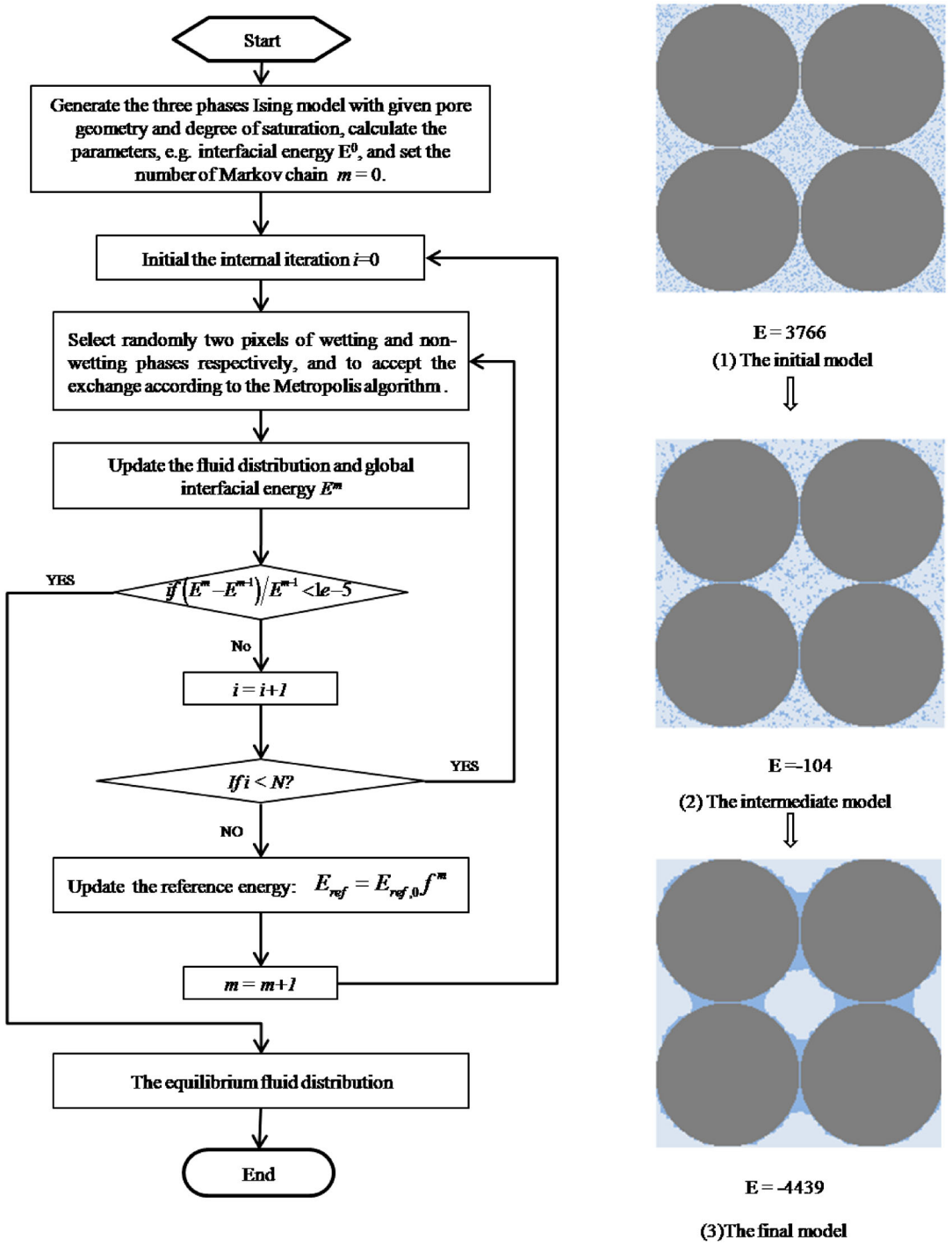

Figure 1. Flowchart of the simulated annealing method for modeling two-phase distributions (N is the number of iterations, which is set as 200 in this paper).

interface, which is called anti-aliasing [22] (Figure 2(d)). The simulated annealing is a commonly used methodology for multi-parameter global optimization problems. More details on the implementation can be found in [16, 22]. There are also some shortcomings of the SAM, for example, (a) the interaction force between different phases is unable to be considered precisely; and (b) the computational requirement is high because of the requirement of global optimization, which also leads to the difficulties in parallel implementation.

Copyright © 2015 John Wiley & Sons, Ltd.

DOI: 10.1002/nag

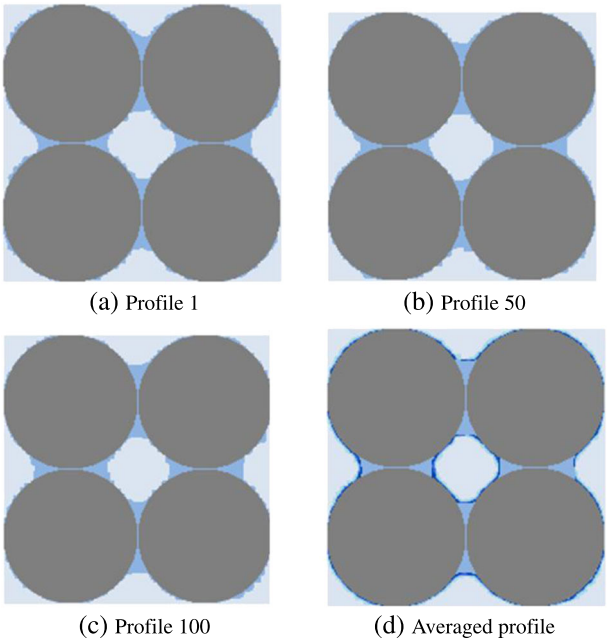

Figure 2. Anti-aliasing to produce a smooth interface after equilibrium is obtained.

2.2. *Lattice Boltzmann method*

2.2.1. Background theory. The LBM is originated from the lattice gas automata where the space, time, and particle velocities are all discrete. Its fundamental idea is to construct a kinetic model to represent the macroscopic averaged properties of the fluid and to take account the essential physical information of the incorporated microscopic processes. Particles with different velocities are residing on the nodes x of a regular lattice, and particle distribution functions $f_i(x,t)$ are defined to describe the occupation of particles with the specific velocity at time t. In one time step, there are two subcalculations, that is, the propagation and the collision. The propagation means particles move to the neighbor node in the direction of their velocities. The collision means particles that arrive at a lattice node will interact with each other, which will change their velocity according to the specific scattering rule. The solving procedure can be viewed as a special finite difference scheme for the kinetic equation of the discrete-velocity distribution function. In recent years, the LBM has been regarded as a promising numerical method to simulate single-phase and multiphase fluids for its remarkable ability in dealing with interfacial dynamics and complex boundaries. For example, the bounce-back algorithm can be directly implemented to realize the non-slip boundary condition; that is, when the particle arrives at a node that was resigned as solid, it will be bounced back to its original position, which has been received the most popularity in LBM simulations. To solve the complicated two-phase fluid problems in porous media, the solid–fluid interfacial force can also be readily considered. In this paper, the two classical multiphase LBM models are adopted to investigate the two-phase distribution problem in fractured porous media.

2.2.2. Multi-component multiphase lattice Boltzmann method. In the MCMP LBM, the two-phase system is represented as two indissolvable components. For each of the two fluid components, a distribution function that satisfies the following evolution function is introduced:

$$f_a^k(\boldsymbol{x}+e_a\Delta t, t+\Delta t) = f_a^k(\boldsymbol{x},t) - \frac{\Delta t}{\tau_k}\left[f_a^k(\boldsymbol{x},t) - f_a^{k,\mathrm{eq}}(\boldsymbol{x},t)\right] \tag{6}$$

where $f_a^k(\boldsymbol{x},t)$ is the kth component density distribution function in the ath velocity direction at site x and at time t, Δt is time step for each iteration, and τ_k is a relaxation time. $f_a^{k,\mathrm{eq}}(x,t)$ is the equilibrium distribution function calculated as

Copyright © 2015 John Wiley & Sons, Ltd.

DOI: 10.1002/nag

$$f_a^{k,\mathrm{eq}}(\boldsymbol{x},t) = w_a\rho_k\left[1+\frac{e_a\cdot u_k^{\mathrm{eq}}}{c_s^2}+\frac{\left(e_a\cdot u_k^{\mathrm{eq}}\right)^2}{2c_s^4}-\frac{\left(u_k^{\mathrm{eq}}\right)^2}{2c_s^2}\right] \tag{7}$$

where $c_s = \Delta x/x\sqrt{3}\Delta tx$, with Δx defined as the lattice spacing. e_a are the discrete velocities in the two dimensional cases and are given by

$$[e_0,e_1,e_2,e_3,e_4,e_5,e_6,e_7,e_8] = \begin{bmatrix} 0 & 1 & 0 & -1 & 0 & 1 & -1 & -1 & 1 \\ 0 & 0 & 1 & 0 & -1 & 1 & 1 & -1 & -1 \end{bmatrix} \tag{8}$$

ω_a are weight indexes defined as

$$\omega_a = \begin{cases} \dfrac{4}{9} & (a=0) \\ \dfrac{1}{9} & (a=1,2,3,4) \\ \dfrac{1}{36} & (a=5,6,7,8) \end{cases} \tag{9}$$

u_k^{eq} is the macroscopic velocity in the equilibrium distribution given by

$$u_k^{eq} = u\text{'} + \frac{\tau_k \boldsymbol{F}_k}{\rho_k} \tag{10}$$

where u' is the composite macroscopic velocity, which is expressed as

$$u' = \frac{\sum_k \frac{1}{\tau_k}\sum f_a^i e_a}{\sum_k \frac{1}{\tau_k}\rho_k} \tag{11}$$

$\boldsymbol{F}_k$ is the interaction force acting on the kth component involving the fluid–fluid cohesion force $\boldsymbol{F}_{\mathrm{c},k}$, fluid–solid adhesion force $\boldsymbol{F}_{\mathrm{ads},k}$, and external force $\boldsymbol{F}_{\mathrm{ext}}$, which is expressed as

$$\boldsymbol{F}_k = \boldsymbol{F}_{\mathrm{c},k} + \boldsymbol{F}_{\mathrm{ads},k} + \boldsymbol{F}_{\mathrm{ext}} \tag{12}$$

The cohesion force acting on the kth component is

$$\boldsymbol{F}_{c,k}(\boldsymbol{x},t) = -G_c\psi_k(\boldsymbol{x},t)\sum_a w_a\psi_{\overline{k}}(\boldsymbol{x}+e_a\Delta t,t)e_a \tag{13}$$

where G_c is the parameter that controls the strength of the cohesion force, and ψ_k and $\psi_{\overline{k}}$ are the interaction potential for the components k and $\overline{k}$, respectively, which can be taken as the density of each component.

The adhesion force acting on the kth component is calculated as

$$\boldsymbol{F}_{\mathrm{ads},k}(\boldsymbol{x},t) = -G_{\mathrm{ads},k}\psi_k(\boldsymbol{x},t)\sum_a w_a s(\boldsymbol{x}+e_a\Delta t)e_a \tag{14}$$

where $G_{\mathrm{ads},k}$ is a parameter that adjusts the interaction strength between the kth fluid component and the solid surface, and $s(\boldsymbol{x}+e_a\Delta t)$ is an indicator function equal to 1 for solid nodes and 0 for fluid nodes.

The external force $\boldsymbol{F}_{\mathrm{ext}}$ acting on the kth component is defined as the body force on the particles (e.g., gravity), which is set as 0 for all simulations.

After every iteration, the distribution function can conveniently be thought of as a typical histogram representing a frequency of occurrence. The frequencies can be considered to be direction-specific

Copyright © 2015 John Wiley & Sons, Ltd.

DOI: 10.1002/nag

fluid densities. Accordingly, the macroscopic density and velocity of the kth component can be obtained as

$$\rho_k = \sum_a f_a^k \tag{15}$$

$$u_k = \sum_a f_a^k e_a / \rho_k \tag{16}$$

2.2.3. Single-component multiphase lattice Boltzmann method. The basic components of the SCMP LBM, such as the evolution function, equilibrium distribution function, macroscopic velocity, and density are similar to MCMP Shan–Chen model. Instead of two distribution functions for each component, only one distribution function is used in the SCMP LBM. The principal distinguishing characteristic of the SCMP LBM is the incorporation of the non-ideal equation of state. In this paper, we employ the equation of state proposed by Shan and Chen [26]:

$$\varphi(\rho) = \varphi_0 \exp(-\rho_0/\rho) \tag{17}$$

where φ_0 and ρ_0 are arbitrary constants that dominate the characteristics of the equation of state.

The cohesion force of gas/water and the adhesion force of fluid/surface in the SCMP LBM are defined as follows:

$$\boldsymbol{F}_c(\boldsymbol{x}, t) = -G_c \psi(\boldsymbol{x}, t) \sum_a w_a \psi(\boldsymbol{x} + e_a \nabla t, t) e_a \tag{18}$$

$$\boldsymbol{F}_{ads}(\boldsymbol{x}, t) = -G_{ads} \psi(\boldsymbol{x}, t) \sum_a w_a s(\boldsymbol{x} + e_a \nabla t) e_a \tag{19}$$

where G_c controls the strength of the cohesion force between two phases and G_{ads} adjusts the interaction strength between the fluids and the solid surfaces.

2.2.4. The Palabos library. The Palabos library [35] is an open-source numerical framework based on the LBM, which was developed by Jonas Latt and co-workers [36]. The Palabos library utilizes generic programming, which means that it allows for the intuitive implementation of LBM models with almost no loss of efficiency and with the ease of further development. Because of the algorithmic parallel nature of LBM, high-efficiency parallel computation has been provided in the Palabos library. In this paper, all computations were performed on Leonardi, which is a medium-sized high-performance computing cluster designed to be used for post-graduate and research purposes within the Faculty of Engineering at the University of New South Wales [37]. It currently consists of 2944 AMD Opteron 6174 2.20-GHz processor cores, with a total of 5.8 TB of physical memory (essentially, 2 GB of memory per core) and 100 TB of usable disk storage. Leonardi runs the Rocks clustering platform on top of CentOS Linux. The parallelization is performed with the message-passing paradigm of the Message Passing Interface (MPI) library, which works well on distributed-memory platforms (e.g., clusters).

For the study of fluid distributions in a fractured porous medium, both the fluid–fluid and fluid–solid interfacial forces are necessary to determine the contact behavior and the interface characteristics. However, in the latest release of Palabos library (May 16, 2013), only the fluid–fluid interface force was provided in the Shan–Chen LBM. It is essential to modify the code so as to involve the fluid–solid interfacial forces. The codes that deal with the fluid–fluid interfacial force can be found in the 'ShanChenprocessor' from the directory of 'multiphysics', which correspond to the implementation of Equations (13) and (18). To include the solid–fluid interfacial forces, Equations (14) and (19) should be programmed in the code. According to Equation (14), three additional parameters are required in the MCMP LBM model: $G_{ads,1}$, $G_{ads,2}$, and *Solid Index*, where $G_{ads,1}$ and $G_{ads,2}$ are the parameters that determine the fluid–solid adhesive force for each of the fluid components and the *Solid Index* is used to indicate the solid nodes. Similarly, two parameters are added in the SCMP

Copyright © 2015 John Wiley & Sons, Ltd.

DOI: 10.1002/nag

LBM model according to Equation (19): G_{ads} and *Solid Index*. In both codes, the contributions of the fluid–solid on the interfacial forces are calculated if any neighbors of the fluid node are recognized as solid nodes. Then, these adhesive forces are added to the original fluid–fluid forces using Equation (12).

To validate the modified Palabos library in dealing with multiphase contact and interaction problems, a single-drop problem with the complete range of contact angle is numerically simulated. For a three-phase system, as shown in Figure 3(a), the wettability of a solid surface (gray) by a liquid (blue) can be characterized by Young's equation [38]:

$$\cos\theta_1 = \frac{\sigma_{2s} - \sigma_{1s}}{\sigma_{12}} \tag{20}$$

where θ_1 is the contact angle between fluid 1 and the solid surface; σ_{1s} and σ_{2s} are the interfacial tensions between fluids 1 and 2 and the solid surface, respectively; and σ_{12} is the interfacial tension between fluids 1 and 2.

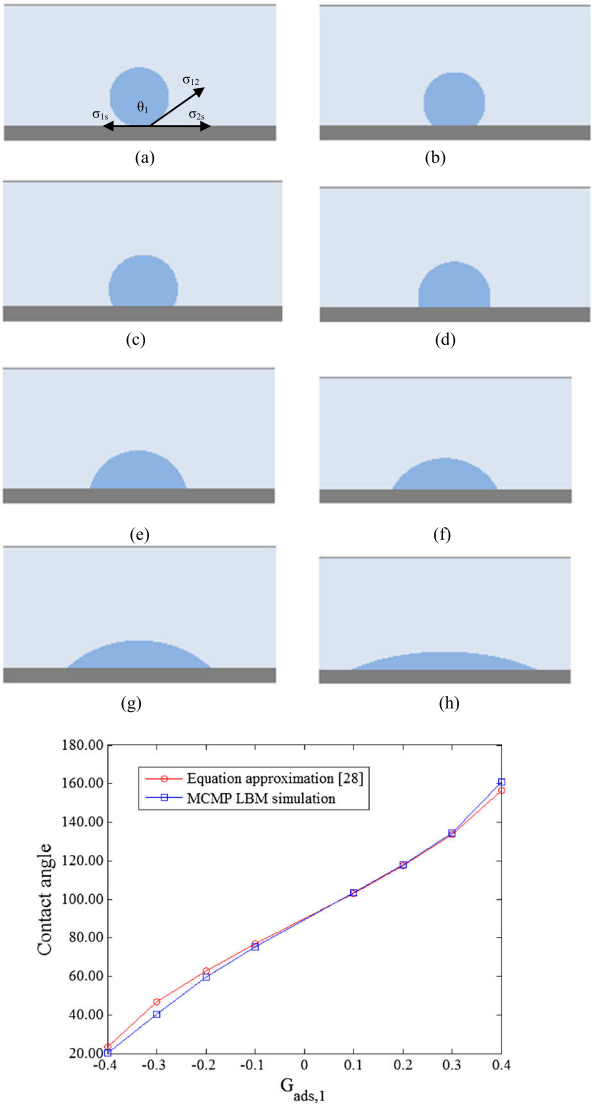

Figure 3. Correlation between G_{ads},σ and the contact angle in the multi-component multiphase (MCMP) lattice Boltzmann method (LBM) ($G = 0.9$; $G_{ads,2} = -G_{ads,1}$).

Copyright © 2015 John Wiley & Sons, Ltd.

DOI: 10.1002/nag

In the MCMP LBM, the interfacial tensions are controlled by the parameters G_c and $G_{ads,k}$. The relation between the contact angle and these parameters is given by Sukop [39] as

$$G_c \cos\theta_1 = G_{ads,2} - G_{ads,1} \tag{21}$$

which was further improved by Huang *et al.* [28] into

$$\cos\theta_1 = \frac{G_{ads,2} - G_{ads,1}}{G_c \frac{\rho_1 - \rho_2}{2}} \tag{22}$$

where ρ_1 is the equilibrium main density and ρ_2 is the associated dissolved density.

For the SCMP LBM, the contact angle between the wetting phase and the solid surface can be estimated according to Lu *et al.* [31] using Equation (23)

$$\theta = 210.75 + 0.647 G_{ads} \tag{23}$$

To simulate the multiphase contact phenomenon, the simulation domain was selected as 200×100 lattice units (l.u.), and the wetting component was initialized as a square with sides of 40 l.u., whereby the wetting component contacts the solid surface. To obtain a reasonable and stable simulation, the lattice space, relaxation time, and time step are chosen as 1, respectively.

In the MCMP LBM models, $\rho_1 = 1.0$ and $\rho_2 = 0.06$ were selected for the sake of stability [28]. $G_{ads,1}$ and $G_{ads,2}$ were chosen in the manner reported in [28], that is, $G_{ads,1}$ varies from -0.4 to 0.4, with $G_{ads,2} = -G_{ads,1}$. Figure 3 shows the complete range of contact angles predicted by the modified Palabos library.

Similar simulations were conducted using the SCMP LBM, in which the parameters φ_0 and ρ_0 in Equation (16) were selected as 200 and 4, respectively, G_c was fixed as -120, and G_{ads} varied between -327 and -40. The initial configuration was set in the same manner as was in the MCMP LBM, and the density of the wetting and non-wetting phases were chosen as 524 and 85, respectively. Figure 4 shows the simulation results predicted by the SCMP LBM [31]. It is clear that the solid–fluid interfacial forces are correctly implemented in the modified Palabos library, and the complete range of contact angles within multiphase systems can be reasonably captured.

3. VERIFICATION

In this section, numerical simulations using three numerical methods, that is, the SAM, MCMP LBM, and SCMP LBM, were conducted for the two-phase fluid distribution problem in [29]. In their work, the contact angle of the wetting phase was selected as 0° to reproduce the near perfect wetting. Therefore, the LBM parameters for the rest of simulations were chosen the corresponding ones in the last section, which can reproduce the zero contact angle.

The solid phase was taken from the micro X-ray CT image (Figure 5(a)). All the simulations (except Figure 5(d)) were initialized with a random distribution of wetting and non-wetting phases in the pore space (e.g., Figure 1(a)). To remove the initial effect on the final conuration of the MCMP LBM, the model in Figure 5(d) was initialized to be the same as one slice of the 3D model shown in Figure 5(b). In all of these simulations, the degree of saturation was set as 0.67 with respect to the wetting phase, and the parameters were selected to produce a zero contact angle [29]. The equilibrium condition is approached when the stored energy converged, more specifically, the ratio between the deviation and average energy of the system less than 10^{-4}.

The simulation results using different numerical methods are shown in Figure 5(c)–(f). To produce a quantitative comparison of the different numerical methods, the lineal-path function [40] was adopted to compare the numerical simulation results with the X-ray micro CT result. The lineal-path function is defined as the probability of finding a line segment that lies entirely in one phase, which contains connectivity information along a lineal path and reflects certain long-range information about the multiphase system. The wetting phase linear path functions of the fluid configuration from different

Copyright © 2015 John Wiley & Sons, Ltd.

DOI: 10.1002/nag

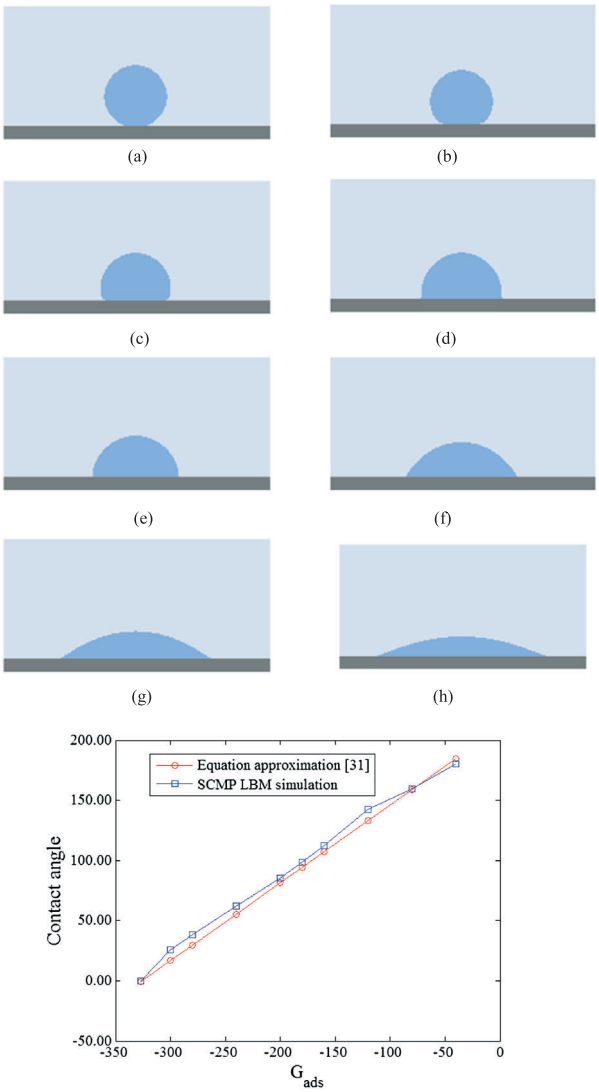

Figure 4. Correlation between G_{ads} and the contact angle in the single-component multiphase (SCMP) lattice Boltzmann method (LBM) ($G = -120$).

methods are illustrated in Figure 6. It can be observed that the numerical simulation results are in good agreement with the experimental data in terms of the stochastic morphological description. However, different conclusions will be obtained when a detailed comparison between the fluid distribution pattern of the center area (Figure 5(a)) is performed. The reason that only center area is considered as the influence of periodic boundary conditions is minimal in the central area. It will be further discussed in Section 4.1.

It is apparent that the results using the MCMP LBM with random initial configurations (Figure 5(c)) are very different compared with the corresponding X-ray results (Figure 5(a)). The best fits are those results using the SAM and the SCMP LBM (Figure 5(e) and (f)). It should be mentioned that the MCMP LBM is sensitive to the initial configuration. For example, when a suitable initial configuration is used, a better result can be generated (Figure 5(d)).

This difference comes from the dependence on the initial configuration. To verify this, we set an initial configuration as the square wetting phase with a non-wetting hole of different radius inside, which is shown in Figures 7(a) and (b) and 8(a) and (b). From Figure 7(d), it is clear that, in the MCMP LBM, the wetting phase (blue part) splits up once the hole is sufficiently large. In contrast, for the SCMP LBM, only one droplet is generated regardless of how large the hole is (Figure 8(c) and (d)).

Copyright © 2015 John Wiley & Sons, Ltd.

DOI: 10.1002/nag

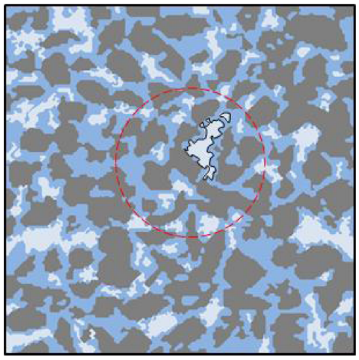

(a) Micro-X-ray CT [29]

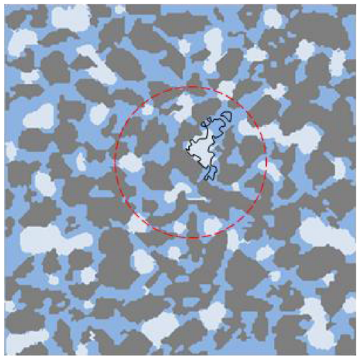

(b) Slice of 3D MCMP Shan-Chen model[29]

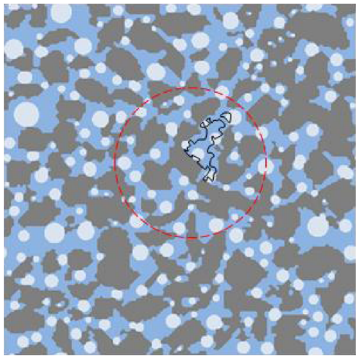

(c) MCMP Shan-Chen model randomly initialized

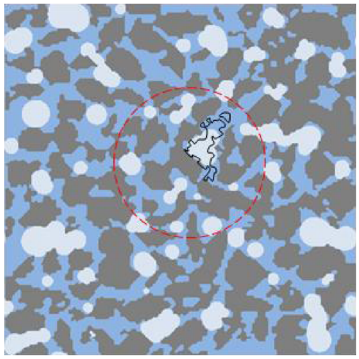

(d) MCMP Shan-Chen model initialized with (b)

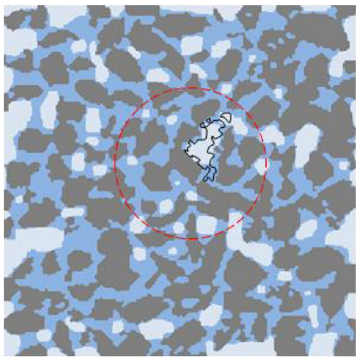

(e) Simulated annealing method

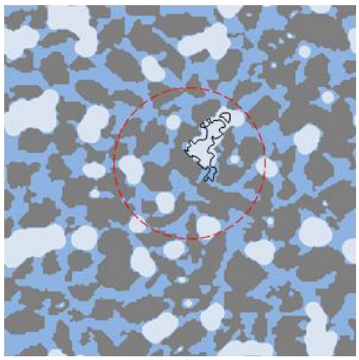

(f) SCMP Shan-Chen model

Figure 5. Comparison between micro X-ray CT and three numerical methods. CT, computed tomography; MCMP, multi-component multiphase; SCMP, single-component multiphase.

Based on the comparison between the numerical results and experimental observations as presented in Figure 7, it can also be revealed that the mechanism of the MCMP LBM is the kinematic movement of the fluids, whereas the SCMP LBM involves both kinematic theory and phase transitions. Meanwhile, the SAM is the optimization approach to obtain the equilibrium distribution as the minimum system energy. Both the SCMP LBM and the SAM can produce very desirable results compared with the experimental observation. This indicates that the process of two-phase fluid distribution within porous media is controlled by both the phase transition and kinematic movement. Therefore, in terms of computational efficiency and mechanism explanation, the SCMP LBM is the most suitable solution. It can simulate a multiphase system with a complete range of contact angles and phase transition. Moreover, its high computational efficiency is another advantage, for example, the MPI parallel computation.

Copyright © 2015 John Wiley & Sons, Ltd.

DOI: 10.1002/nag

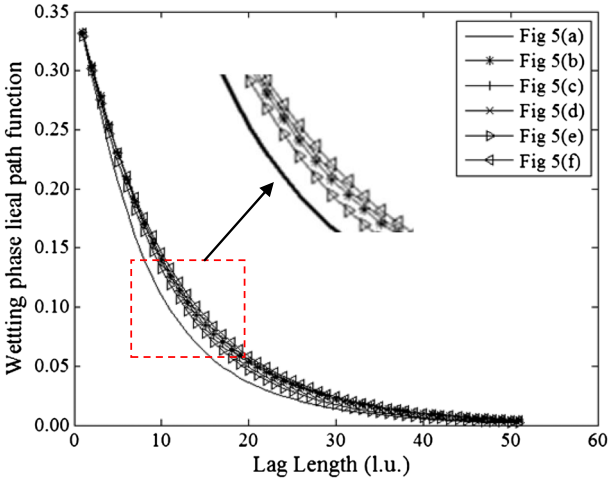

Figure 6. Wetting phase linear-path function of different fluid distributions by the different methods in Figure 5.

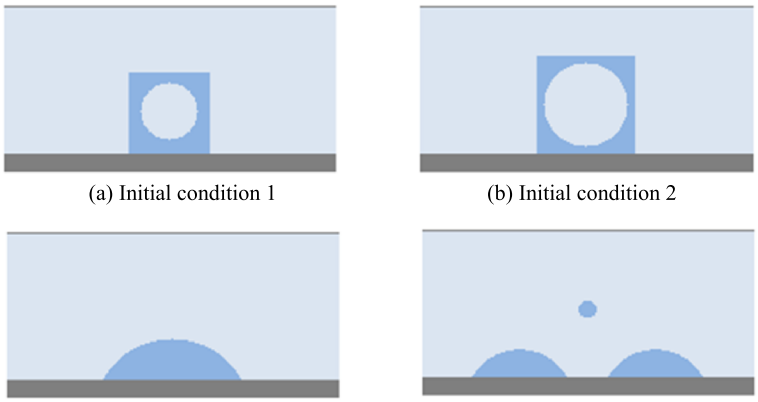

(a) Initial condition 1 (b) Initial condition 2

(c) Final configuration from (a) (d) Final configuration from (b)

Figure 7. Dependence on the initial configuration in the multi-component multiphase (MCMP) Shan–Chen model.

4. TWO-PHASE FLUID DISTRIBUTION IN FRACTURED POROUS MEDIA

4.1. Periodic boundary effect and initial configurations

Various boundary conditions in the LBM have been proposed and evaluated [36, 41–43]. The 'periodic' boundary condition has usually been applied at the model's edges for the sake of simplicity [27]. However, this will introduce some errors because porous media are not geometrically 'periodic' under most conditions. In this paper, the influence of periodic boundary conditions on the simulation results of the SCMP LBM on fluid distribution problems is investigated. The porous media are generated through the compaction of randomly sized particles using the discrete element method code PFC^{2D} [44]. A total of 557 particles with radii 30−50 l.u. are generated in the 2000 × 2000 l.u. domain. In order to produce the hydraulic aperture and create well-connected pore space in the random compaction system, the radii of the particles are reduced to 80% of its original size, but the centers are kept the same as the initial position. The final geometry of the porous media is shown in Figure 9(a), with radii of 24−40 and porosity of 0.552. During the SCMP LBM simulation, all the parameters are set in the way that follows Table I. A number of sub-

Copyright © 2015 John Wiley & Sons, Ltd.

DOI: 10.1002/nag

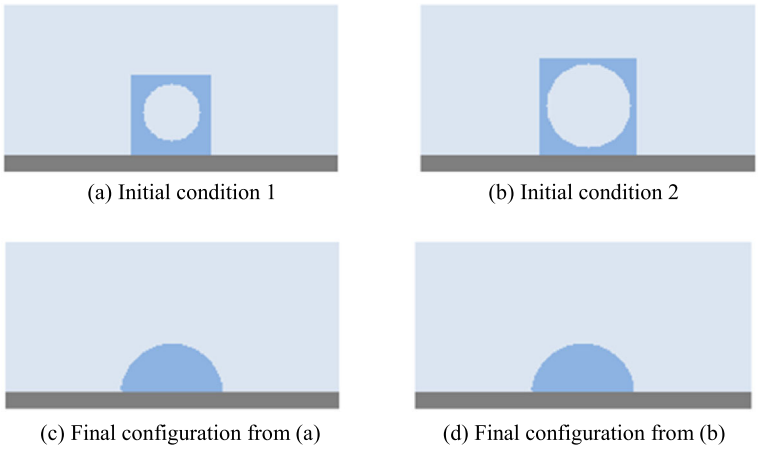

Figure 8. Dependence on the initial configuration in the single-component multiphase (SCMP) Shan–Chen model.

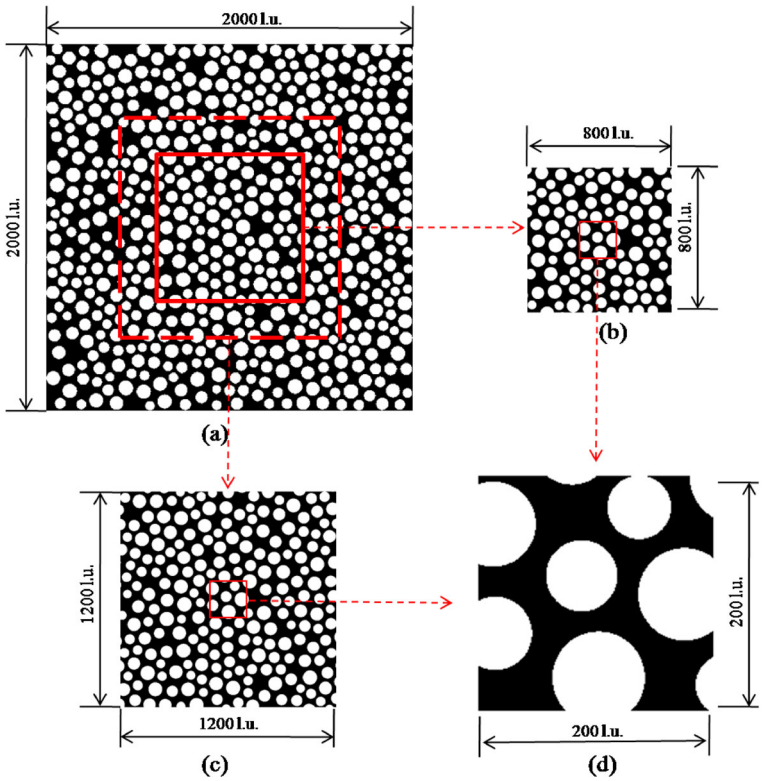

Figure 9. Geometry of a porous medium generated from discrete element method. (a) The whole region of the porous medium; ((b) and (c)) two examples of different buffer sizes, and (d) the region of interest.

models with different sizes were cropped from the original model (e.g., Figure 9(b) and (c)). The purpose is to find a suitable model size to minimize the influence of the 'periodic boundary' over the region of interest (Figure 9(d)). The macroscopic properties, degree of saturation, and specific surface area (SSA) of the two-phase fluid interface of the region of interest are shown in Figure 10. It can be found that the macroscopic properties of the numerical simulation are only slightly influenced by the 'periodic boundary' when the model size is sufficiently large, which confirms its applicability to fluid distribution simulations. It should be mentioned that the simulations are

Copyright © 2015 John Wiley & Sons, Ltd.

DOI: 10.1002/nag

Table I. Parameters used in the single-component multiphase lattice Boltzmann method simulations.

Boundary condition at open ends	Periodic
Boundary condition at the solid nodes	Bounce back
Contact angle	0 (perfect wetting)
φ_0	200
ρ_0	4
G_c	−120
G_{ads}	−327
Density of wetting phase	524
Density of non-wetting phase	85
Relaxation time (τ)	1
Time step	1
Lattice space	1

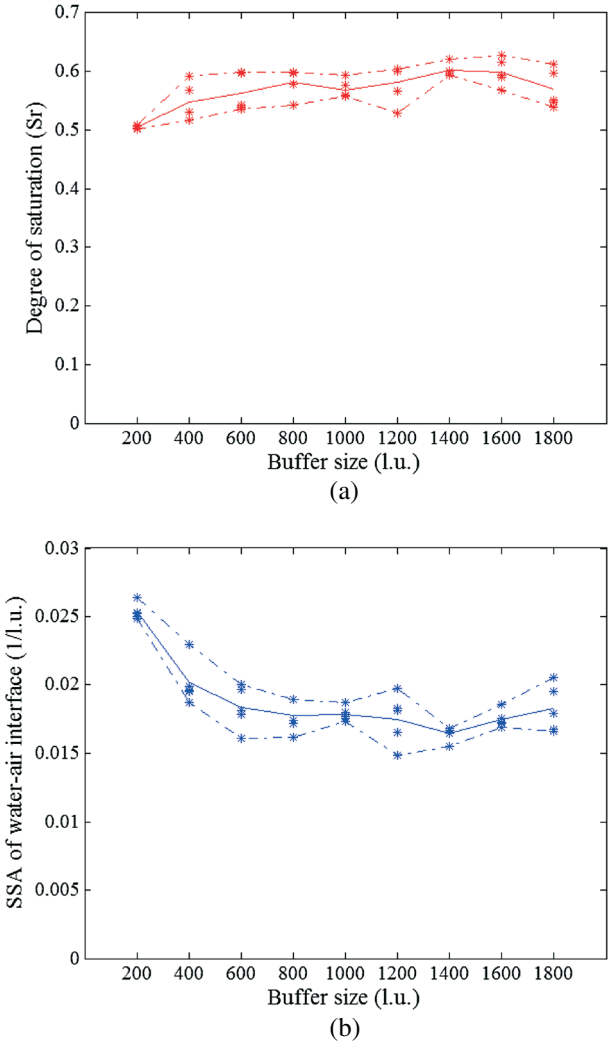

Figure 10. Influence of buffer size on the macroscopic properties in the region of interest. SSA, specific surface area.

conducted in the same geometry for five runs to reduce the stochastic effects of the random initial configurations, which will be addressed later. Moreover, the difference in the fluid configuration in the region of interest is also slight with increased model size (Figure 11). However, when the

Copyright © 2015 John Wiley & Sons, Ltd.

DOI: 10.1002/nag

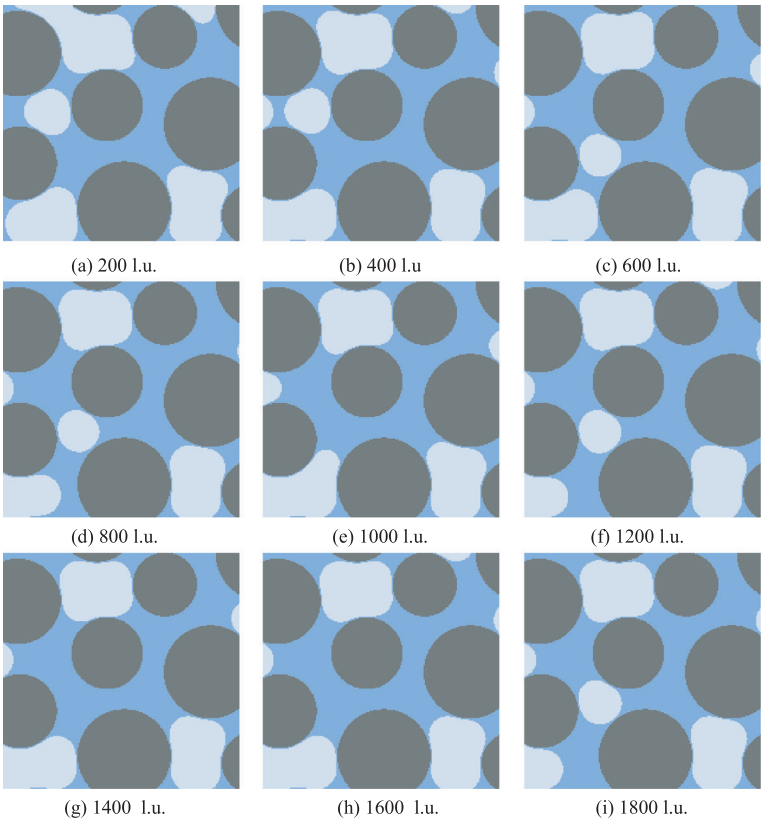

Figure 11. Fluid distribution in the region of interest from simulations of different buffer sizes.

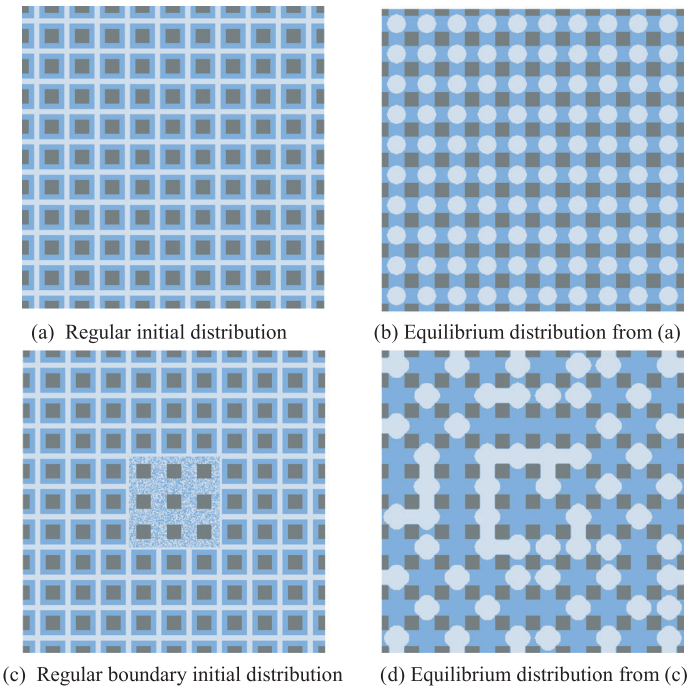

Figure 12. Investigation of the boundary conditions and the initial configuration.

Copyright © 2015 John Wiley & Sons, Ltd.

DOI: 10.1002/nag

'periodic boundary' is directly applied to the region of interest, an apparent difference will be generated (Figure 11(a)); therefore a buffer area is recommended. From Figures 10 and 11, it is found that if the buffer size is large than 4001.u., the degree of saturation and the SSA of water–air interface become

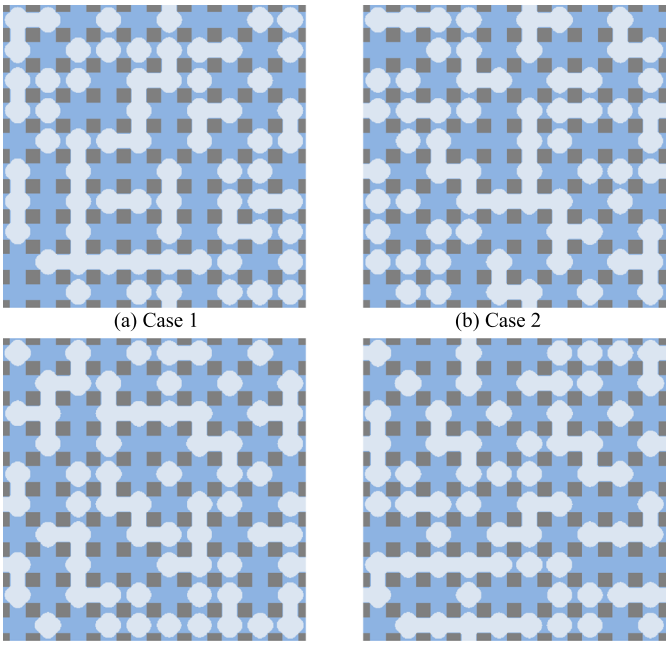

Figure 13. Fluid distribution in regular geometry from different random initializations.

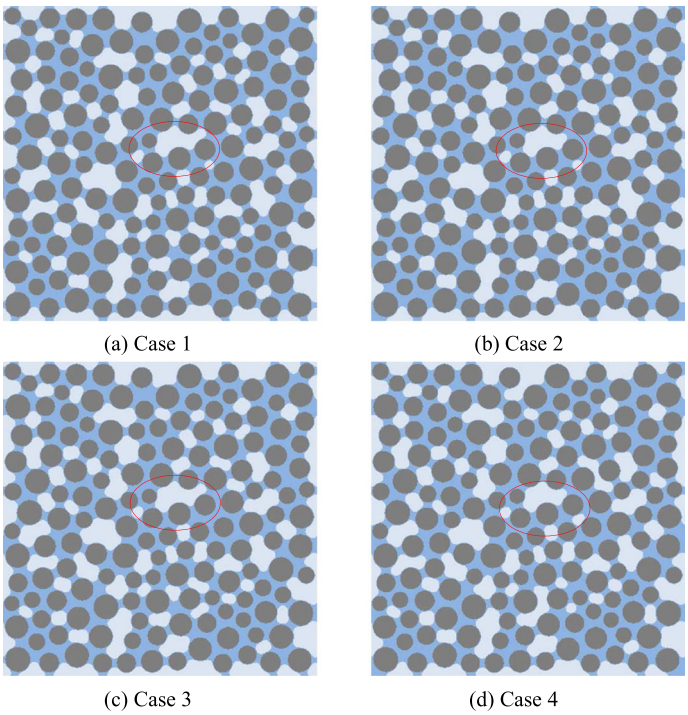

Figure 14. Fluid distribution in irregular geometry from different random initializations.

Copyright © 2015 John Wiley & Sons, Ltd.

DOI: 10.1002/nag

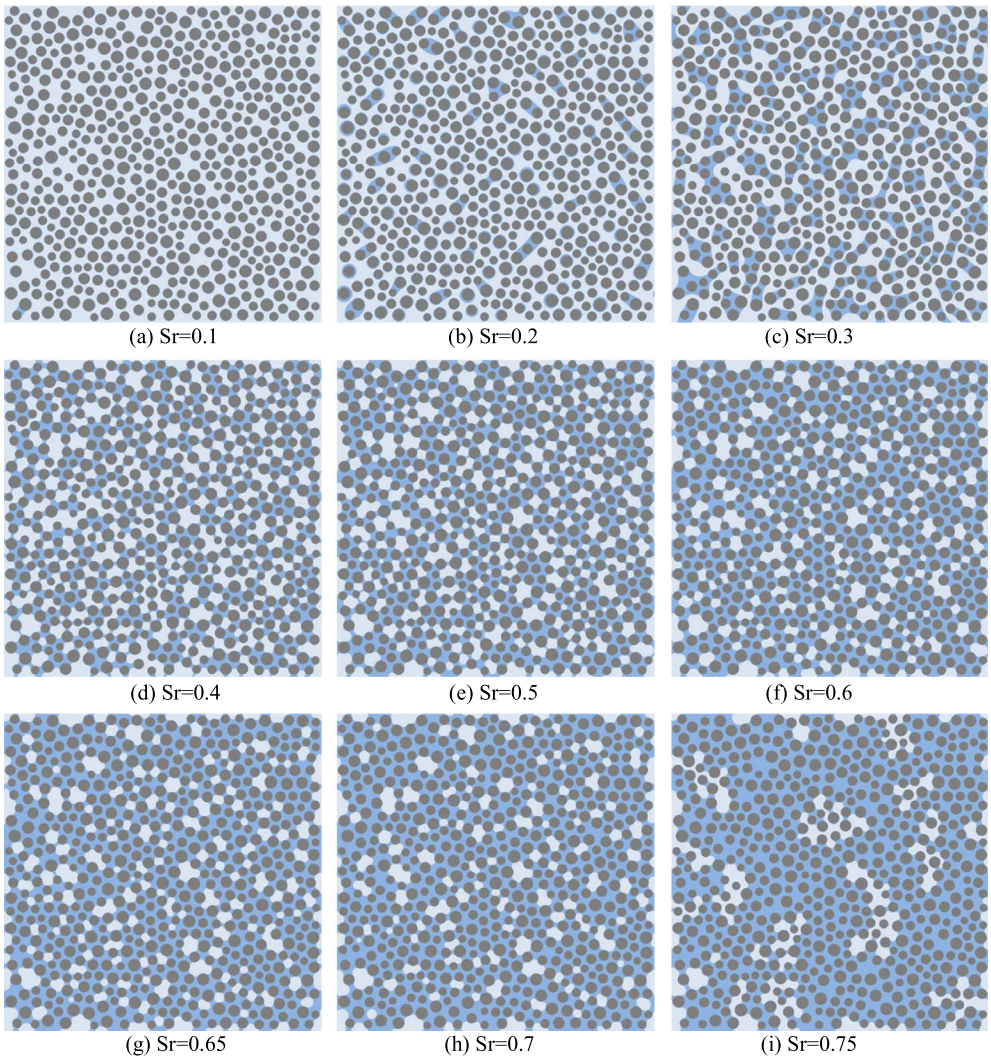

Figure 15. Multiphase distribution at different degrees of saturation in a porous medium.

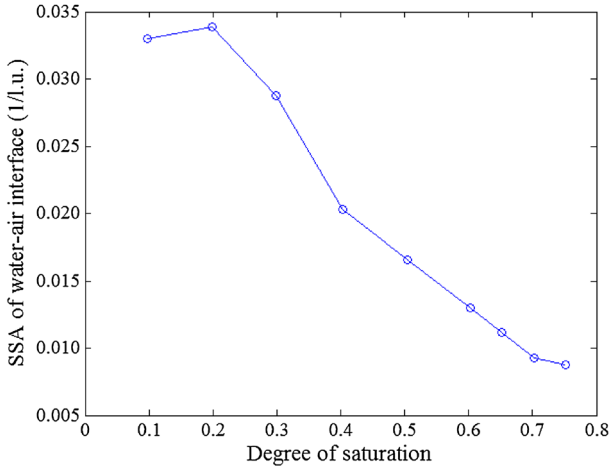

Figure 16. Correlation between the degree of saturation and the specific surface area of the fluid interface. SSA, specific surface area.

Copyright © 2015 John Wiley & Sons, Ltd.

DOI: 10.1002/nag

relatively stable. By considering the average particle size in the generated porous media as 32 l.u., the minimum simulation size is suggested, taken as about 12.5 times of the average particle radii so as to reduce the periodic boundary effect and obtain accurate distribution.

To study the influence of the initial fluid distribution, a model with regular solid squares enveloped by a water film with the same thickness is first simulated (Figure 12(a)). Because the model geometry is perfectly 'periodic', the boundary condition will not introduce any error, which can be confirmed from the modeling results shown in Figure 12(b), where a perfect homogeneous fluid distribution pattern is obtained. In the following, the middle part of the regular configuration is replaced by a random distribution for the initial configuration (Figure 12(c)); for this case, the periodic boundary condition is still fulfilled. However, a clearly different distribution pattern is obtained (compare with Figure 12(b)). Therefore, it can be concluded that for regular porous media, the initial distribution will significantly influence the fluid distribution patterns. For example, all the models are randomly initialized in the middle part and simulated four times, and Figure 13 shows the final distributions, where a large difference in the distribution patterns is presented in the regular system. The same simulation is performed for irregular porous media (Figure 14), where only slight differences can be observed. It is easy to draw the conclusion that the initial distribution is less sensitive to irregular porous media (e.g., geomaterials) compared with regular media.

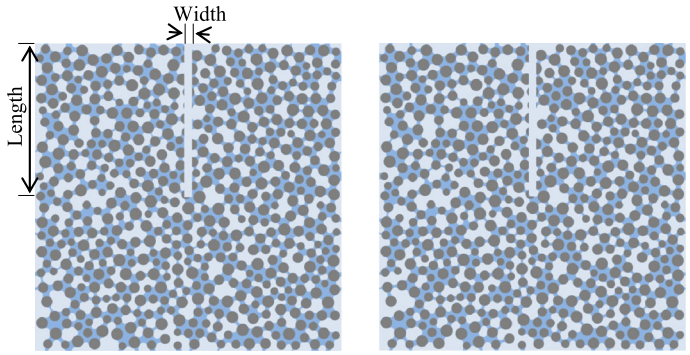

Figure 17. Influence of fractures on multiphase distributions ($S = 0.4$, fracture width = 100 l.u., fracture length = 1000 l.u.).

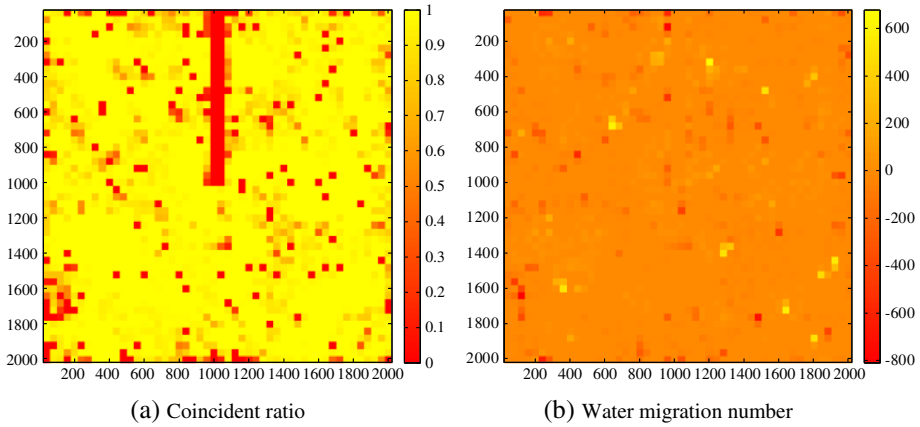

Figure 18. Macroscopic description of differences between Figure 17(a) and (b) ($S = 0.4$, fracture width = 100 l.u., fracture length = 1000 l.u.).

Copyright © 2015 John Wiley & Sons, Ltd.

DOI: 10.1002/nag

4.2. *Fluid distribution in porous media*

In this section, the influence of saturation on the fluid configuration in porous media is studied using the SCMP LBM. The solid part of the system remains the same as in Figure 9(a); the parameters are chosen to produce zero contact angle for the wetting phase, as reported in the last section; and the degree of saturation of the wetting phase varies from 0.1 to 0.75.

The simulated distribution patterns are shown in Figure 15. It is clear that, at very low degrees of saturation (Figure 15(a)), the solid phase is enveloped by the wetting films. The wetting films become thicker as the saturation increases, and capillary condensation between particles is produced (Figure 15(b)). A connected network of the wetting phase can be obtained at certain degrees of saturation (Figure 15(e)). When the degree of saturation continues increasing, large portions of the porous medium become occupied by the wetting phase, and most of the non-wetting phase is trapped in the large pores, as observed in Figure 15(i). The simulated results are in agreement with the experimental observations from the X-ray CT images in both the assembling glass beads and Ottawa sand under different degrees of saturation from Lu *et al*. [22]. Moreover, the SSAs of the fluid interfaces are calculated at different degrees of saturation (Figure 16). The SSA of the interfaces increase as the degree of saturation becomes less than 0.2, and the opposite phenomenon is observed when the degree of saturation becomes larger than 0.2. The overall trend, first increasing and subsequently decreasing, also agrees well with the experimental observations in Lu *et al*. [22].

4.3. *Fluid distribution in fractured porous media*

For a porous medium with a static fluid distribution, by introducing fractures, the fluid distribution will evolve to a new equilibrium condition. In this section, the influence of the fracture length and width on the fluid changes in the porous media under different degrees of saturations (Sr) will be investigated using the SCMP LBM. During the simulation, the equilibrium fluid distribution of the porous medium under given Sr is first calculated. Then, a fracture with given length and width will be

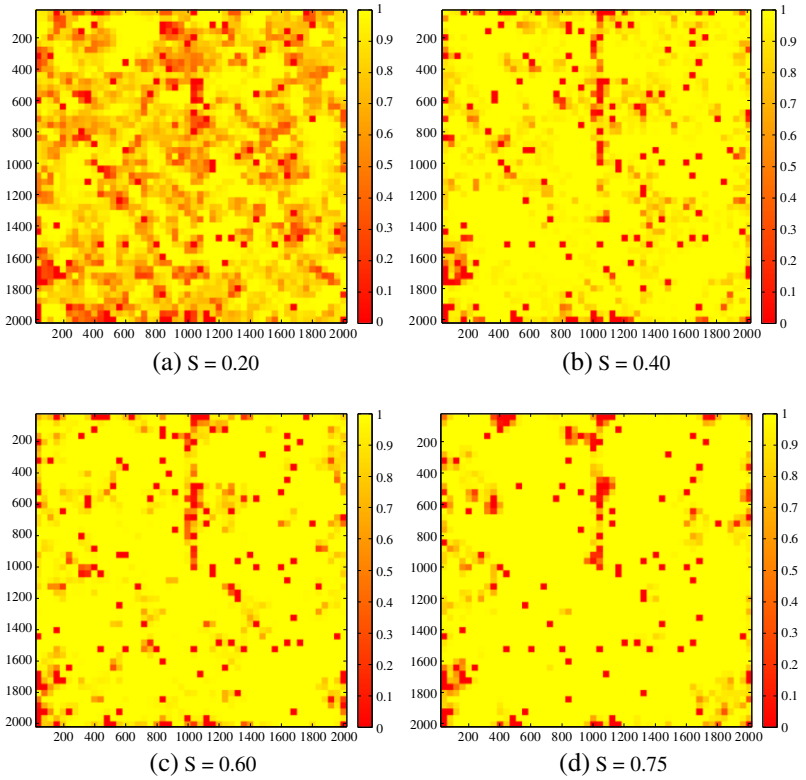

Figure 19. Influence of the degrees of saturation on the coincident ratio (fracture width = 50 l.u., fracture length = 1000 l.u.).

Copyright © 2015 John Wiley & Sons, Ltd.

DOI: 10.1002/nag

inserted into the model (Figure 17(a)). To implement this in the LBM model, all the nodes including the solid, wetting, and non-wetting phases in the range of fracture are converted to the non-wetting phase (e.g., air). The model will not be at equilibrium, which leads to the fluid migration. Using the SCMP LBM, the final equilibrium condition can be obtained (Figure 17(b)). By conducting a large number of simulations, the influence of fractures on the fluid distribution can be observed using the numerical results. In this paper, the parameters are chosen as follows: Sr with respect to the wetting phase = 0.2, 0.4, 0.6, and 0.75; the fracture width = 25, 50, 75, and 100 l.u.; and the fracture length = 500, 1000, 1500, and 2000 l.u.

It should be mentioned that the fluid flow distribution in fractured porous media is geometrically irregular and unsuitable for direct analysis; for example, it is difficult to find the fluid migration using Figure 17. To obtain a more quantitative analysis, the simulation domain is further divided into $N_{\text{sub}} \times N_{\text{sub}}$ sub-regions. The coincident ratio at sub-region i is defined as

$$\text{Coincident ratio}_{(i)} = \frac{N_{\text{co}(i)}}{N_{\text{wetting}(i)}} \tag{24}$$

where $N_{\text{co}(i)}$ and $N_{\text{wetting}(i)}$ are the number of coincident wetting phases (two pixels of the original porous medium and the fractured porous medium at the same location were both wetting) and the number of pixels in the wetting phase at sub-region i of the original porous medium, respectively. This index can represent the disturbance of the wetting phase; that is, if it is equal to 1, then there is no disturbance, and if it is equal to 0, then the wetting phase is completely disturbed (migrated).

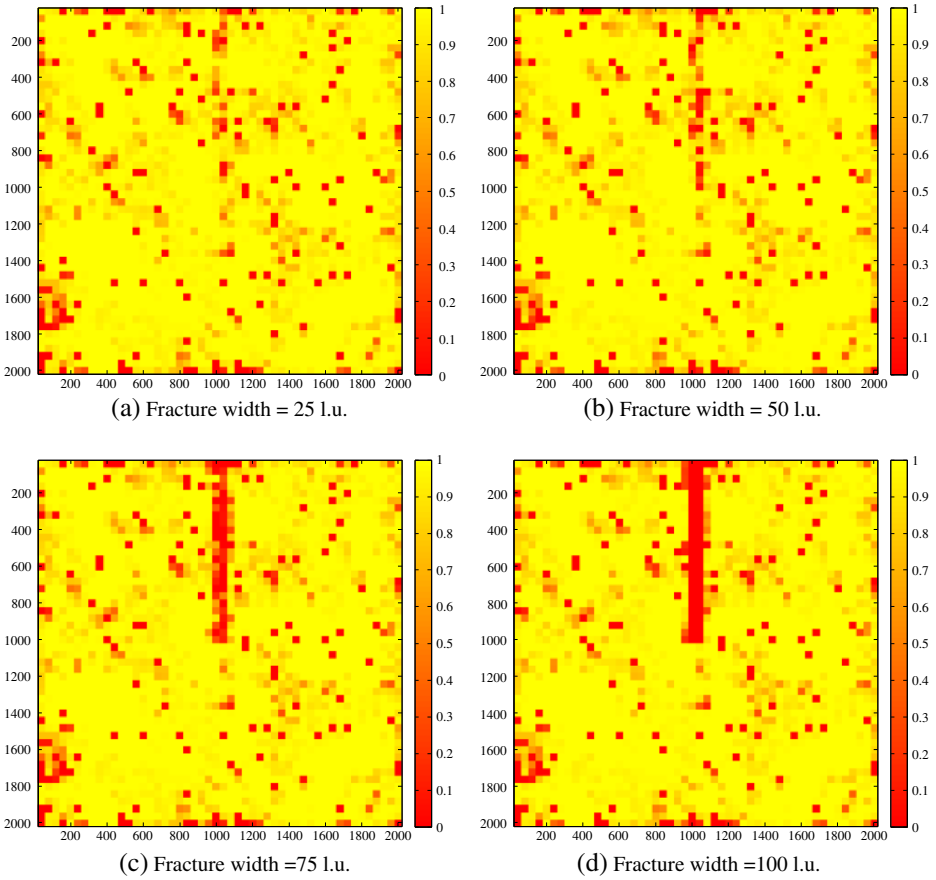

(a) Fracture width = 25 l.u. (b) Fracture width = 50 l.u.

(c) Fracture width =75 l.u. (d) Fracture width =100 l.u.

Figure 20. Influence of the fracture widths on the coincident ratio ($S = 0.4$, fracture length = 1000 l.u.).

Copyright © 2015 John Wiley & Sons, Ltd.

DOI: 10.1002/nag

Another index, the water migration number, is defined as the amount of change in the wetting phase at the sub-region and is given as

$$\text{Water migration number}_{(i)} = N'_{\text{wetting}(i)} - N_{\text{wetting}(i)} \tag{25}$$

where $N'_{\text{wetting}(i)}$ and $N_{\text{wetting}(i)}$ are the numbers of wetting phase pixels in the wetting phase at sub-region i of the fractured and initial porous media. It is a positive value for flowing in and a negative value for flowing out.

The purpose of the postprocessing is to present information of fluid migration produced in the LBM simulation. The sub-region size is like the view of the observer: when the size is too small (e.g., 1 l.u.), the N_{co} would be 1 or 0, and the whole image would be the shape of the immigrated water. However, when the view is too large, for example, the whole model, it would be a single value for the whole model, which is close to 0. Therefore, for both too large and too small, the postprocessed results are not of our interest. The size is selected as the small order of the fracture size and particle size, in order to observe the index as a whole, and also could reflect the influence of presentence of fracture on the fluid distribution. In this paper, the size of sub-region is selected as squares with side lengths of 40×40 l.u. Therefore, the total number of 50×50 sub-regions is divided.

The changes in the two-phase distribution induced by the fracture expressed as the coincident ratio and water migration number in each sub-region are shown in Figure 18. It can be found that the fracture can apparently be reflected from the contour map of the coincident ratio calculated at each sub-region (Figure 18(a)); in contrast, it is unable to be distinguished using the water migration number (Figure 18(b)). Therefore, the coincident ratio is used as the postprocessing for the simulation

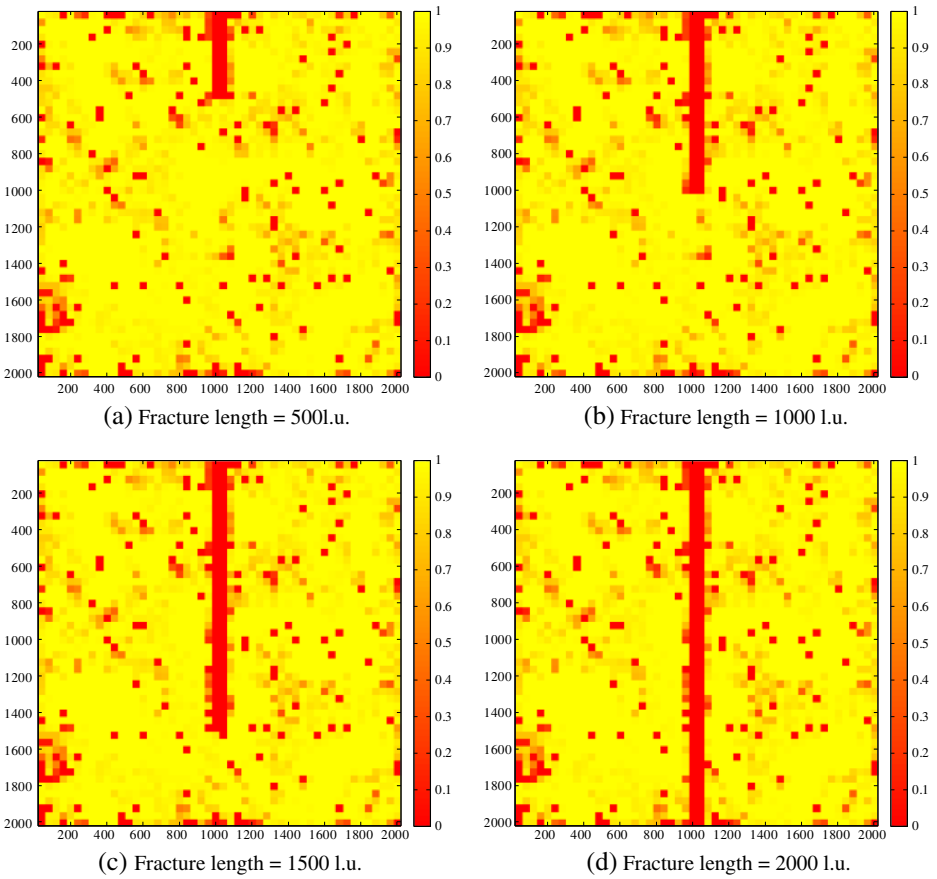

Figure 21. Influence of fracture lengths on the coincident ratio ($S = 0.4$, fracture width = 100 l.u.).

Copyright © 2015 John Wiley & Sons, Ltd.

DOI: 10.1002/nag

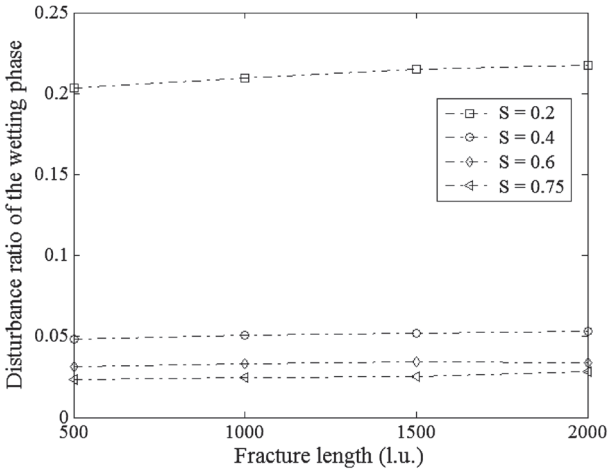

(a) Fracture width = 25 l.u.

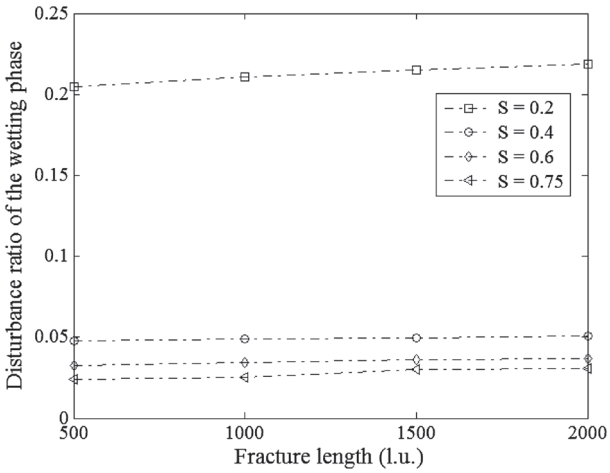

(b) Fracture width = 100 l.u.

Figure 22. Influence of the fracture length on the disturbance ratio at different degrees of saturation.

results. The influences of saturation, fracture width, and fracture length on the two-phase fluid distributions are diagramed in Figures 19–21, respectively. A large part of the system is disturbed at low degrees of saturation (Figure 19(a)), and the disturbance area decreases as the degree of saturation increases (Figure 19(b)–(d)). The disturbance area increases with increasing width and length of the fracture, with most of the disturbance occurring around the fracture, as illustrated in Figures 20 and 21.

To quantify the disturbed region of the whole model due to the induced fracture, a disturbance ratio Ω is introduced as follows:

$$\Omega = 1 - \frac{\sum N_{\mathrm{co}(i)}}{\sum N_{\mathrm{wetting}(i)}} \tag{26}$$

The influences of the fracture length, fracture width, and degree of saturation on the disturbance ratio are summarized in Figure 22. It can be observed that the disturbance ratio increases with the fracture length. Meanwhile, it is also found that the disturbance ratio decreases as the degree of saturation increases. A possible application of these numerical findings is to explore fractures (which might be too small to be observed through X-ray CT due to the limitation of resolution) by indirectly investigating the fluid distribution. Furthermore, it is widely accepted that the fluid

Copyright © 2015 John Wiley & Sons, Ltd.

DOI: 10.1002/nag

distribution will influence the flow behaviors within a multiphase system. However, it is not practical to obtain the fluid distribution with limited information. Therefore, the most important contribution is that a feasible solution for two-phase flow distribution using the SCMP LBM is verified, which can be further used to prepare a more reliable initial fluid distribution for analysis of two-phase flow behavior in fractured porous media.

5. CONCLUDING REMARKS

To sum up, the SCMP LBM is found to be the best method in predicting the fluid distribution in partially saturated porous media compared with two other methods (the SAM and the MCMP LBM). The effect of periodic boundary conditions and the initial configuration is also tested. It is found that a buffer size of approximately 12.5 times the average particle size is suggested to reduce the error resulting from the periodic boundary conditions. Moreover, the initial distribution of the SCMP LBM is less sensitive for an irregular porous medium than that of a regular medium; therefore, it is more suitable for natural porous media, such as rock and soil. The influence of the degree of saturation on the two-phase fluid distribution was investigated using this method. The fluid distribution patterns and the quantitative evaluation at different degrees of saturation were investigated, which are consistent with experimental results from the literature. Finally, the influence of fractures on the two-phase fluid distribution was also studied. The disturbance ratio is introduced to evaluate the change in the two-phase system due to the induced fracture. It was found that more fluids are disturbed as the fracture length and width increase, and the disturbance ratio decreases as the degree of saturation increases.

ACKNOWLEDGEMENTS

This research is financially supported by the Australian Research Council (grant nos. DE130100457 and DP130104918).

REFERENCES

1. Jim-Douglas JR, Spagnuolo AM. The transport of nuclear contamination in fractured porous media. *Journal of the Korean Mathematical Society* 2001; **38**(4):7263–7764.
2. Trivedi J, Babadagli T. Experimental and numerical modeling of the mass transfer between rock matrix and fracture. *Chemical Engineering Journal* 2009; **146**:194–204.
3. Sudicky EA, Frind EO. Contaminant transport in fractured porous media: analytical solutions for a system of parallel fractures. *Water Resources Research* 1982; **18**(6):1634–1642.
4. Or D, Tuller M. Liquid retention and interfacial area in variably saturated porous media: upscaling from single-pore to sample-scale model. *Water Resources Research* 1999; **35**(12):3591–3605.
5. Gray WG, Tompson AFB, Soll WE. Closure condition for two-fluid flow in porous media. *Transport in Porous Media* 2002; **47**:29–65.
6. Culligan KA, Wildenschild D, Christensen BSB, Gray WG, Rivers ML, Tompson AFB. Interfacial area measurements for unsaturated flow through a porous medium. *Water Resources Research* 2004; **40**:W12413.
7. de Gennes PG, Brochard-Wyart F, Quere D. *Capillary and Wetting Phenomena*. Springer: New York, 2003; 291 pp.
8. Reynodls DA, Kueper BH. Multiphase flow and transport through fractured heterogeneous porous media. *Journal of Contaminant Hydrology* 2004; **71**(1–4):89–110.
9. German ER, Akin S, Castanier L. Multiphase flow properties of fracture porous media. *Journal of Petroleum Science and Engineering* 2006; **51**:197–213.
10. Gvirtzman H, Magaritz M, Klein E, Nadler A. A scanning electron microscopy study of water in soils. *Transport in Porous Media* 1987; **2**:83–93.
11. Schmitz D, Reinecke N, Petritsch G, Mewes D. X-ray computed tomography for stationary multiphase flow in random and structured packings. Conference Proceedings: Frontiers in Industrial Process Tomography II. 1997. Delft.
12. Schmitz D, Reinecke N, Petritsch G, Mewes D. High resolution X-ray tomography for stationary multiphase flows. OECD/CSNI Specialist Meeting on Advanced Instrumentation and Measurement Techniques.1997.Santa Barbara
13. Wildenschild D, Cullingan KA, Christensen BSB. Application of X-ray microtomography to environmental fluid flow problems. Proc. SPIE 5535, Developments in X-Ray Tomography IV, 432 (October 26, 2004)
14. Liaw HK, Kulkarni R, Chen S, Watson AT. Characterization of fluid distribution in porous media by NMR techniques. *AIChE Journal* 1996; **42**(2):538–546.
15. Krummel A, Datta SS, Münster S, Weitz DA. Visualizing multiphase flow and trapped fluid configurations in a model three-dimensional porous medium. *AIChE Journal* 2013; **59**:1022.

Copyright © 2015 John Wiley & Sons, Ltd.

DOI: 10.1002/nag

16. Kirkpatrick S, Gelatt CD, Vecchi MP. Optimization by simulated annealing. *Science, New Series* 1983; **220**(4598): 671–680.
17. Politis MG, Kainourgiakis ME, Kikkinides ES, Stubos AK. *Application of Simulated Annealing on the Study of Multiphase Systems, Simulated Annealing 1998*, Cher Ming Tan (ed.). InTech: Rijeka, Croatia, 2008; 207–226, ISBN: 978-953-7619-07-7, InTech.
18. Knight R, Chapman A, Knoll M. Numerical modeling of microscopic fluid distribution in porous media. *Journal of Applied Physics* 1990; **68**(3):994–1001.
19. Silverstein DL, Fort T. Prediction of air–water interfacial area in wet unsaturated porous media. *Langmuir* 2000; **16**:829–834.
20. Silverstein DL, Fort T. Prediction of water configuration in wet unsaturated porous media. *Langmuir* 2000; **16**:83–844.
21. Berkowitz B, Hansen DP. A numerical study of the distribution of water in partially saturated porous rock. *Transport in Porous Media* 2001; **45**:303–319.
22. Lu N, Zeidman BD, Lusk MT, Willson CS, Wu DT. A Monte Carlo paradigm for capillarity in porous media. *Geophysical Research Letters* 2010; **37**:L23402.
23. Chen S, Doolen GD. Lattice Boltzmann method for fluid flows. *Annual Review of Fluid Mechanics* 1998; **30**:329–364.
24. Huang HB, Wang L, Lu X. Evaluation of three lattice Boltzmann models for multiphase flows in porous media. *Computers and Mathematics with Applications* 2011; **61**:3606–3617.
25. Shan X, Chen H. Lattice Boltzmann model for simulating flows with multiple phases and components. *Physical Review E* 1993; **47**:3.
26. Shan X, Chen H. Simulation of nonideal gases and liquid–gas phase transitions by the lattice Boltzmann equation. *Physical Review E* 1994; **49**:4.
27. Pan C, Hilpert M, Miller CT. Lattice Boltzmann simulation of two phase flow in porous media. *Water Resources Research* 2004; **40**:W01501. doi:10.1029/2003WR002120.
28. Huang HB, Thorne DT, Schaap MG, Sukop MC. Proposed approximation for contact angles in Shan-and-Chen-type multicomponent multiphase lattice Boltzmann models. *Physical Review E* 2007; **76**:066701.
29. Sukop MC, Huang HB, Lin CL, Deo MD, Oh K, Miller JD. Distribution of multiphase fluids in porous media: comparison between lattice Boltzmann modeling and micro-x-ray tomography. *Physical Review E* 2008; **77**:026710.
30. Sukop MC, Or D. Invasion percolation of single component, multiphase fluids with lattice Boltzmann models. *Physica B* 2003; **338**:298–303.
31. Lu G, Wang XD, Duan YY. Study on initial stage of capillary rise dynamics. *Colloids and Sufaces A: Physicochemical and Engineering Aspects.* 2013; **433**:95–103.
32. Zimmerman RW, Bodvarsson GS. Hydraulic conductivity of rock fractures. *Transport in Porous Media* 1996; **23**:1–30.
33. Wang JSY, Narasimhan TN. Hydrologic mechanisms governing fluid flow in partially saturated, fractured, porous medium. *Water Resources Research* 1985; **21**(12):1861–1874.
34. Cipra B. An introduction to the Ising model. *American Mathematics Monthly* 1987; **94**:937–959.
35. 2009; http://www.palabos.org/ (accessed on 16 May 2013).
36. Latt J, Chopard B, Malaspinas O, Deville M, Michler A. Straight velocity boundaries in the lattice Boltzmann method. *Physical Review E* 2008; **77**:056703.
37. 2011; http://leonardi.unsw.wikispaces.net/home (accessed on 01 July 2014).
38. Adamson AW, Cast AP. *Physical Chemistry of Surfaces*. John Wily & Sons: Inc New York, 1997.
39. Sukop MC, Thorne DT. *Lattice Boltzmann Modeling: An Introduction for Geoscientists and Engineers*. Springer-Verlag: Berlin/Heidelberg, 2006.
40. Hilfer R. Local porosity theory and stochastic reconstruction for porous media. *Statistical Physics and Spatial Statistics* 2000. K. Mecke and D. Stoyan, Springer: Berlin Heidelberg. **554**:203–241.
41. Ziegler DP. Boundary conditions for lattice Boltzmann simulations. *Journal of Statistical Physics* 1993; **71**:1171–1177.
42. Inamuro T, Yoshino M, Ogino F. A non-slip boundary condition for lattice Boltzmann simulations. *Physics of Fluids* 1995; **7**:2928–2930.
43. Zou Q, He X. On pressure and velocity boundary conditions for the lattice Boltzmann BGK model. *Physics of Fluids* 1997; **9**:1591–1598.
44. Cundall PA, Strack ODL. A discrete numerical model for granular assemblies. *Geotechnique* 1979; **29**(1):47–65.

Copyright © 2015 John Wiley & Sons, Ltd.

DOI: 10.1002/nag

View publication stats